Research Square

Preprints are preliminary reports that have not undergone peer review. They should not be considered conclusive, used to inform clinical practice, or referenced by the media as validated information.

In Vivo Multimodal Retinal Imaging Correlates With Granular-specific Changes in the Organelles of Retinal Pigment Epithelium of a Murine Model of Stargardt Disease

Ratheesh K. Meleppat
University of California Davis
Kaitryn E. Ronning
University of California Davis
Sarah J. Karlen
University of California Davis
Marie E. Burns
University of California Davis
Edward N. Pugh
University of California Davis
Robert J. Zawadzki (rjzawadzki@ucdavis.edu)
University of California Davis

Research Article

Keywords: Multimodal Retinal Imaging, Stargardt Disease, Pigment Epithelium

Posted Date: June 10th, 2021

DOI: https://doi.org/10.21203/rs.3.rs-590253/v1

License: This work is licensed under a Creative Commons Attribution 4.0 International License.
Read Full License

Version of Record: A version of this preprint was published at Scientific Reports on August 10th, 2021. See the published version at https://doi.org/10.1038/s41598-021-95320-z.

Loading [MathJax]/jax/output/CommonHTML/jax.js

Abstract

Melanosomes, lipofuscin, and melanolipofuscin are the three principal types of granular pigmented organelles found in the retinal pigment epithelium (RPE) cells. Changes in the density of melanosomes and lipofuscin granules in RPE cells are considered hallmarks of various retinal diseases, including Stargardt disease and age-related macular degeneration (AMD). Herein, we report the potential of an *in vivo* multimodal imaging technique based on directional back-scattering and short-wavelength fundus autofluorescence (SW-FAF) to study the disease-related changes in the density of melanosomes and lipofuscin granules in RPE cells. Changes in the concentration of these granules in *Abca4*$^{-/-}$ mice (a model of Stargardt disease) relative to age-matched wild-type (WT) controls were investigated. Directional optical coherence tomography (dOCT) was used to assess the melanosome density *in vivo*, whereas the AF images and emission spectra acquired with a spectrometer-integrated scanning laser ophthalmoscope (SLO) were used to characterize the lipofuscin and melanolipofuscin granules in the same RPE region. Subcellular-resolution *ex vivo* imaging using confocal fluorescence microscopy and electron microscopy was performed on the same tissue region to visualize and quantify melanosomes, lipofuscin, and melanolipofuscin granules. Comparisons between *in vivo* and *ex vivo* results confirmed an increased concentration of lipofuscin granules and decreased number of melanosomes in the RPE of *Abca4*$^{-/-}$ mice and provided an explanation for the differences in fluorescence and directionality of RPE scattering observed *in vivo* in the two mouse strains.

Introduction

The retinal pigment epithelium (RPE) is a monolayer of pigmented cells located posterior to the photoreceptors of the neurosensory retina. The RPE plays a critical role in metabolic and transport functions essential for neuronal homeostasis, and RPE dysfunction leads to photoreceptor degeneration and contributes to a variety of retinal diseases, including age-related macular degeneration (AMD)[1,2]. Therefore, the ability to perform noninvasive, *in vivo* evaluation of the RPE state is of great interest to clinical ophthalmology and ophthalmic research. RPE organelles, predominantly melanosomes and lipofuscin, undergo morphological and biochemical changes with age and disease, and thus could serve as biomarkers for aging and progression of diseases of the outer retina.

Lipofuscin granules are the brightly fluorescent granules found in the lysosomal compartment of the RPE and are a result of the phagocytosis of the distal tips of the photoreceptor outer segments[3]. Lipofuscin is a heterogeneous mixture of lipid-containing residues of lysosomal digestion and exhibits characteristics autofluorescence from the constituent bisretinoid compounds[4]. The most prominent component of these bisretinoid compounds, N-Retinyl-N-retinylidene ethanolamine (A2E), has been found to have toxic effects on RPE cell functions [3,5,6]. It has been widely reported that accumulation of RPE lipofuscin, and in particular A2E, plays a detrimental role in degenerative retinal diseases, including AMD and Stargardt disease [7,8]. A hallmark of the Stargardt disease is a premature accumulation of lipofuscin due to the defects in the ABCA4 transporter, which normally acts to remove N-Retinyl-N-retinylidene phosphatidyl-

Loading [MathJax]/jax/output/CommonHTML/jax.js

ethanolamine from the inner leaflet of photoreceptor disc membranes [9–11]. Similar excessive accumulation of lipofuscin is found in Abca4 knockout (*Abca4*$^{-/-}$) mice, a model widely used for the preclinical investigation of Stargardt disease [11–13].

The melanosome is an organelle in which melanin is synthesized and stored in pigmented cells. Melanosomes in the RPE are formed during embryonic development and mature during early postnatal stages, while lipofuscin and melanolipofuscin granules, which are a mixture of the two precursor granules, accumulate as a function of age. Melanosomes serve to protect the RPE from light damage and light-generated oxygen reactive species [14,15]. Melanosomes have been observed to undergo morphological and photophysical alterations with age, possibly due to oxidation, decreasing their antioxidation potential[16,17]. The density of the RPE melanosomes is also reported to decline with the increased lipofuscin load (caused by age or disease), where the melanosomes tend to fuse with lipofuscin granules forming melanolipofuscin [17,18]. Thus, *in vivo* monitoring of the changes of melanosomes and lipofuscin granules in the RPE is of prominent clinical interest.

Short-wavelength fundus autofluorescence (SW-FAF) imaging (excitation ~ 488 nm and emission > 500 nm), has been widely used for monitoring lipofuscin accumulation in RPE. SW-FAF imaging is generally performed with a confocal scanning laser ophthalmoscope (cSLO) since the confocal optics allows the acquisition of an AF signal from the RPE complex while rejecting AF from interior parts of an eye such as the lens and cornea. However, the accuracy of the intensity-based SW-FAF assessment is limited due to its dependence on multiple factors such as the position of the focal plane in respect to the RPE layer, ocular transmission, data acquisition, gain, AD conversion, image processing, and variation between the systems [19,20]. Assessment based on the spectral profile (shape) of the emission spectrum could overcome most of the above limitations with intensity-based SW-FAF and provide more evidence for the characterization of lipofuscin and its changes.

Near-infrared fundus autofluorescence (NIR-FAF) imaging (excitation ~ 785 nm, emission > 810 nm) is used for monitoring changes in melanin in the outer retina [21,22]. In addition to the inherent issues with confocal optics, overlapping strong NIR-FAF from choroidal melanosomes with emission of RPE melanosomes complicates the accurate assessment of RPE melanosomes. Over the last decade, optical coherence tomography (OCT) has emerged as a gold standard for clinical retinal diagnostics due to its unique ability to provide high contrast, depth-resolved morphology of the retinal layers *in vivo* with micrometer resolution [23,24]. Clinical OCT systems use near-infrared (NIR) light (centered at ~ 850 nm or ~ 1050 nm) to detect the back-scattered light from the retinal layers to generate cross-sectional images. Back-scattered light from the retinal layers can also provide critical information regarding tissue properties and underlying changes with diseases[25–29]. In a recent study using mouse models with varying melanin pigmentation levels, we showed that directional reflectivity (directional back-scattering) of the RPE layer, when measured with a directional OCT (dOCT), is directly linked with the RPE melanin concentration [27]. This result showcases directional RPE scattering as a potential biomarker for various [illegible] e density of RPE melanosomes. Therefore, measuring

Loading [MathJax]/jax/output/CommonHTML/jax.js

directional reflectance together with SW-FAF signal (images and spectra) of RPE could provide critical complementary information regarding organelle specific changes of the granular melanosomes and lipofuscin in RPE.

In this paper, we report an *in vivo* multimodal investigation based on directional back-scattering (directional reflectivity) and SW-FAF, that reveals the changes in the density of lipofuscin granules and melanosomes in the RPE of a 14-month-old *Abca4*$^{-/-}$ mouse (a model of Stargardt disease) relative to age-matched wild-type (WT). *In vivo* observations were linked with microscopic observations of RPE organelles obtained with multiple *ex vivo* imaging methods. The same regions of RPE were imaged *in vivo* with a swept source-based dOCT system to acquire directional back-scattering and with a spectrometer-integrated SLO system to acquire AF spectra and fundus images. The *in vivo* results were correlated with *ex vivo* imaging results from the same animals and regions where *in vivo* imaging was performed.

Materials And Methods

Animal models and preparation for in vivo imaging

All animal procedures were performed with approval by the University of California, Davis Institutional Animal Care and Use Committee (IACUC). The study was conducted in accordance with all relevant guidelines and regulations, including the National Institute of Health (NIH), the Association for Research in Vision and Ophthalmology (ARVO), and Animal Research: Reporting of In Vivo Experiments (ARRIVE). A cohort of 14-month-old pigmented (agouti background) WT (129S1/SvlmJ) and age-matched *Abca4*$^{-/-}$ (129S-Abca4$^{tm1Ght/J}$) mice were used in this study. Both strains were purchased from the Jackson Laboratory (Sacramento, California, USA, strain #002448 and #023725). Both eyes of three WT and three *Abca4*$^{-/-}$ mice were imaged for the *in vivo* studies; no animals, experimental units, or data points were excluded from analysis. During *in vivo* imaging, each mouse was placed on a micropositioner (Bioptigen, Durham NC, USA) that allowed rotational and translational adjustment of the mouse with respect to the SLO/OCT imaging system. During image and spectrum acquisition, mice were anesthetized with the inhalational anesthetic isoflurane (2% in O_2). Pupils were dilated with 1% tropicamide and 2.5% phenylephrine (Akorn, Inc., Lake Forest, Illinois, USA), and the corneal surface was wetted with Gel Tears hypromellose gel (GenTeal Tears, Severe, Alcon, Texas, USA).

In vivo **multimodal imaging**

The multimodal assessment of RPE based on dOCT and SLO-based AF were not acquired simultaneously, but rather with two separate custom imaging systems. To the best of our ability, the dOCT and SLO data were acquired from the same retinal eccentricity. Additionally, the two imaging systems were located side-by-side in our lab, and we performed dOCT and AF imaging one after another under the same experimental conditions.

Loading [MathJax]/jax/output/CommonHTML/jax.js

In vivo **assessment of the directional reflectivity**

A swept-source OCT-based dOCT system was setup to measure the directional reflectivity of RPE and other retinal layers *in vivo* as previously described [27]. In brief, the swept-source (Excelitas Technologies Corp., Waltham, Massachusetts, USA) used for OCT imaging has a center wavelength of ~ 1060 nm and bandwidth of ~ 100 nm. The comprehensive details of the assessment of the directional reflectivity of retinal layers with our dOCT system have been reported previously [27]. The directional reflectivity of RPE/BrM complex and other layers was calculated from the dOCT B-scans. DOCT images of the retina were acquired by moving the position of the imaging beam with respect to the dilated mouse pupil using motorized linear stages. The lateral displacement of the OCT beam changes the angle of illumination of the retina, resulting in tilting of the OCT images (dOCT images). The angle of incidence at each pupil position was calculated from the acquired B-scan after converting the image to 1:1 aspect ratio in axial and transversal directions. The entrance pupil position was shifted to a maximum of 800 μm on either side of the pupil center with a step of 100 μm in orthogonal directions: Horizontal (H) and Vertical (V). Five closely spaced (2 μm separation) OCT B-scans were acquired (total separation between first and last B-scan of ∼8 μm) at each pupil position along the Y direction (orthogonal to laser scanning) and averaged. The length of all B-scans was 20° field of view (FOV) which corresponds to approximately 680 μm in the X and Y direction (scanning) respectively. The averaged B-scans collected from each beam entry position were next tilt-corrected using affine transform and registered using ImageJ (Stack Reg)[30]. From each tilt-corrected B-scan, twenty well-aligned intensity A-scan profiles were selected near the center region and averaged for further analysis. To ensure that the variation in directional reflectivity of RPE/BrM complex between strains was induced only by the changes in melanosomes density, directional reflectivity of other melanin-free retinal layers, such as inner limiting membrane (ILM), external limiting membrane (ELM), and inner-outer segment (IS/OS) junction were also measured and compared. The directional reflectivity of these layers was calculated from averaged A-scan profiles. The measured values of reflectivity as a function of angle of incidence were fitted with a gaussian function provided in Eq. (1).

$$I(x) = a_0 + a_1 * 10^{-\rho[(x-x_0)^2+(y-y_0)^2]}$$

1

Where α_0 and α_1 represent the nondirectional (background) and directional components of retina reflection, respectively. ρ is the directionality parameter. x_0 and y_0 represent the geometric center of the pupil of the dilated eye. The sensitivity of the directional reflection of retinal layers was quantified using a directionality parameter (ρ) from equation (1). The parameter ρ is inversely proportional to full-width-at-half-maximum (FWHM) of the fitted Gaussian function. Therefore, a wider profile (larger FWHM) gives a small value of ρ, and vice versa.

In vivo **autofluorescence measurement**

Loading [MathJax]/jax/output/CommonHTML/jax.js

The SW-FAF images and emission spectra were acquired *in vivo* using a custom-built SLO integrated with a spectrometer (QE 65000, Ocean Optics, Florida, USA)[31]. The SLO system allows the acquisition of FAF images and spectra from any discrete region of interest of the fundus. The fundus images and emission spectra were acquired using 488 nm excitation with a power of 105 μW at the mouse pupil. A high-pass spectral filter with a cut-off wavelength of 503 nm (Semrock, New York, USA) was used as an emission filter. The AF spectra were measured from the same location where the dOCT imaging was performed. The weak FAF signals were amplified with a photomultiplier tube and a gain controller (Hamamatsu H7422-50, Japan). The integration time for the spectrometer was set to 2.5 sec for all the spectral acquisition. The stray fluorescence from the optical elements and dark-leakage current from the detector were recorded separately (without the mouse eye) and subtracted from the fundus AF spectra measured from the mouse. During the collection of fluorescence emission spectra, the fundus regions containing blood vessels and optic nerve head were excluded to ensure that emission is solely contributed by the fluorophores in the RPE.

Preparation of retina flat-mount for ex vivo confocal studies

After completion of *in vivo* imaging, mice were euthanized by CO_2 narcosis, and one eye was enucleated. The enucleated eye was placed in a petri dish containing an ice-cold solution of DMEM (Dulbecco's Modified Eagle Medium, with high glucose and no phenol red, Thermo Fisher 21-063-029) supplemented with 10% fetal bovine serum (FBS, Corning 35010CV) and NucBlue nuclear probe (2 drops per ml of solution, Molecular Probes Thermo Fisher R37605). The eyecup was shaped similar to a four-leaf clover after removing the anterior segment, lens, muscles, and connective tissues on the back of the sclera, and the optic nerve. The retina was then gently peeled off from the eyecup, exposing the RPE layer which remained attached to the choroid and sclera. This latter preparation was placed scleral side down onto a translucent membrane (Whatman 110614). The flat-mount tissue on the membrane was transferred to a Lab-Tek II Chambered Coverglass (Thermo Fisher 155379PK), and placed RPE-side down directly on the cover glass. A custom weighted mesh was placed on top of the membrane, and then fresh, ice-cold DMEM supplemented with 10% FBS was added to the chambered coverglass. The chambered coverglass was then placed on the stage of the Nikon A1 confocal microscope fitted with a LiveCell Stage Top Incubation System (Pathology Devices). For the duration of imaging, the LiveCell system was set to maintain temperature at 36°C, humidity at 60%, and CO_2 at 10%.

Ex vivo **confocal imaging of the flat-mounted RPE**

The high-resolution *in situ* confocal images of the flat-mounted RPE of both strains were acquired with a Nikon A1 confocal microscope (New York, USA) as previously described[32]. Both confocal fluorescence images and emission spectra were acquired at 488 nm excitation. The confocal images were acquired with and without an emission filter in the detection path. A 60 X objective lens (Nikon, Plan Apo VC 60X, Water Immersion) with a numerical aperture of 1.2 was used to acquire confocal image stacks. Twenty-seven confocal planes were acquired from RPE tissue in Z-direction (depth) with a step size of 0.5 μm. NIS-Elements AR processing software was used for all processing and analysis of the confocal images

Loading [MathJax]/jax/output/CommonHTML/jax.js

and emission spectra. 3D image stacks were deconvolved with the confocal point spread function to correct confocal artifacts and chromatic aberration. The 'spectral unmixing' feature of the software was used for the segmentation and quantification of individual fluorophores within the RPE volume.

Ex vivo **imaging with electron microscopy**

Electron microscopy (EM) images of the RPE were acquired with a transmission electron microscope (TEM). Euthanized mice were transcardially perfused with 2% paraformaldehyde, 2% glutaraldehyde, and 0.05% calcium chloride in 50 mM MOPS, pH 7.4 [33]. The eye was enucleated, and the cornea and lens were removed. The posterior eye cup was post-fixed 2 hours then rinsed with PBS. The tissue was blocked, then rinsed in 0.1M sodium phosphate buffer, stained with 1% osmium tetroxide, rinsed in dH20, and dehydrated with an increasing series of ethanol. Blocked tissue was placed in a pre-inflitrate of 50% propylene oxide and 50% PolyBed resin overnight, then infiltrated with 100% PolyBed resin and polymerized in fresh resin. Thin sections (80-90nm) were cut on an ultramicrotome, collected on copper slot grids, and stained with 4 % uranyl acetate and 0.3% lead citrate in 0.1N sodium hydroxide and examined with a Talos L120C TEM. The morphological features of melanosomes, lipofuscin, and melanolipofuscin granules were identified and classified from EM images using the "ParticlePicker " plugin available with ImageJ software [34]. For the quantification of each type of organelles, granules were manually marked with colored dots in a new map based on their actual center location in the EM image using a custom MATLAB script.

Statistical Analysis

PRISM (Version 7.02; GraphPad Software, La Jolla, CA, USA) was used for statistical analysis. Results were presented as mean with standard error (SE) of three mice per group unless otherwise specified. The null hypothesis was that the groups were not statistically different. Two-group comparisons were performed with ANOVA, and a p-value of 0.05 or less was considered statistically significant.

Results

Directional scattering from the RPE layer.

Directional retinal OCT imaging was performed in both mouse strains at a similar retinal eccentricity (distance from ONH) as depicted in *en face* OCT fundus images shown in Fig. 1(a) and (b). The SSOCT system (axial resolution ~ 7.5 μm in air) visualized major retinal boundaries/layers of two mouse strains such as ILM/NFL, outer plexiform layer (OPL), ELM, IS/OS junction, and RPE/BrM (Fig. 1(c) and (d)). Imaging distal tips of the photoreceptors outer segment was not possible with the system due to the limited axial resolution.

DOCT images of retinas of both mouse strains were acquired by varying beam entry positions at the pupil (varying angles of incidence) on the retina along vertical (V) and horizontal (H) directions (Fig. 2). This movement of the pupil entry position results in tilt in the B-scans. The average tilt of the B-scan was

Loading [MathJax]/jax/output/CommonHTML/jax.js

measured to be approximately 3 degrees for every 100 μm of lateral displacement at the entrance pupil position. Acquired dOCT images showed that the reflectivity of many retinal layers depends on the angle of incidence, and visibility of these structures varies as a function of the angle of illumination.

The reflectivity of the retinal layers was quantitatively measured from the averaged A-scan profile extracted from the dOCT images (Fig. 3). The multiple peaks that appeared in the A-scan profiles provided the position and magnitude of the reflectivity of hyperreflective layers such as ILM, OPL, ELM, IS/OS junction, and RPE/BrM complex. The RPE/BrM complex showed the highest peak (reflectivity) among all layers and varied most with angle of incidence.

The incident angle-dependent reflectivity of RPE/BrM complex and other three layers (ILM, ELM, IS/OS) of both strains were measured from A-scan profiles and fitted with a Gaussian function (Fig. 4). The directionality parameter (ρ) of different retinal layers was obtained from Gaussian function using Eq. (1). Table 1 lists the mean and standard error of the directionality parameter measured for different retinal layers in both strains. A large value of the directionality parameter represents a narrow reflectivity profile, which implies a highly directional scattering. Consistent with our previous observations, scattering from the ILM/NFL and ELM was highly directional, whereas the IS/OS junction in both strains exhibited a wider reflectivity profile (Fig. 4 (a) and (b). Furthermore, the directionality parameters measured for ILM/NFL, ELM and IS/OS (which lack melanosomes) are similar and do not statistically differ between the two mouse strains ($p = 0.27$). However, the directional reflectivity profile of the RPEs of the two strains showed a significant difference ($p = 0.01$). The Gaussian profile obtained from WT is wider than *Abca4*$^{-/-}$ mice. The average directionality parameter of RPE/BrM complex measured for *Abca4*$^{-/-}$ mice is nearly 4-fold higher than for WT.

Table 1
Mean value of directionality (ρ) with standard error

Layers	*Abca4*$^{-/-}$		WT	
	H	V	H	V
ILM/NFL	0.240 (± 0.025)	0.232 (± 0.022)	0.265 (± 0.018)	0.274 (± 0.014)
ELM	0.222 (± 0.025)	0.219 (± 0.057)	0.247 (± 0.015)	0.263 (± 0.011)
IS/OS	0.018 (± 0.010)	0.023 (± 0.004)	0.026 (± 0.005)	0.039 (± 0.008)
RPE/BrM	0.171 (± 0.013)	0.184 (± 0.025)	0.041 (± 0.015)	0.052 (± 0.012)

Loading [MathJax]/jax/output/CommonHTML/jax.js

FAF images and emission spectra acquired *in vivo* from WT and *Abca4*$^{-/-}$ are shown in Fig. 5. Figures 5(a) and (b) are the representative FAF images obtained from the WT and *Abca4*$^{-/-}$, respectively. Figures 5(c) and 5(d) represent the *in vivo* recorded AF spectra from the fundus area (shown in red dashed box) of the WT and *Abca4*$^{-/-}$, respectively. There was a notably increased intensity (brightness) of the AF from *Abca4*$^{-/-}$ mice compared to WT, approximately 3.4-fold higher. Additionally, a significant "red" shift in the fluorescence emission spectrum was observed in the *Abca4*$^{-/-}$ relative to the WT.

Ex vivo **fluorescence confocal images**

High-resolution confocal images of RPE flat-mounts from WT and *Abca4*$^{-/-}$ mice were acquired with 488 nm excitation (Figs. 6). Confocal images of the RPE flat-mounts were obtained with and without an emission filter in the microscope detection path. Figures 6(a) and 6(c) show representative confocal images (depth projected) acquired from WT and *Abca4*$^{-/-}$ mice, respectively, without an emission filter. Lack of emission filter permitted the measurement of back-scattered light from RPE resulting in the visualization of both green-colored and spindle-shaped melanosomes (thick white solid arrows) and golden-yellow-colored spherical lipofuscin granules (white hollow arrows)[32]. Figures 6(b) and 6(d) represent the confocal images acquired with an emission filter inserted in the detection channel of the microscope. The melanosomes are not visible in these images because the scattered light from the melanosomes is fully blocked by the emission filter, so only AF signal reaches the spectral detector. The bottom panel of each confocal image represents the side view of the RPE confocal volume. Consistent with our previous observations, melanosomes were predominantly located at the apical side of the RPE (dashed white arrow) and lipofuscin granules occupied the basal region of the RPE (solid thin arrow)[32].

Qualitative and quantitative analyses revealed material differences in the density of the melanosomes and lipofuscin granules (number of granules per picolitre) between *Abca4*$^{-/-}$ and WT controls. There is a reduction in the density of melanosomes in the RPE of *Abca4*$^{-/-}$ relative to WT. In contrast, the number of lipofuscin granules in the *Abca4*$^{-/-}$ is significantly greater than in the WT. The average density of the lipofuscin granules and melanosomes were calculated from the RPE confocal volumes (Fig. 6(e) and 6(f)). The density of lipofuscin granules is approximately 4.2 times higher in *Abca4*$^{-/-}$ than in WT mice, whereas the density of melanosomes declined in *Abca4*$^{-/-}$ mice by a factor 4.7 compared to WT mice.

The normalized average emission spectra from 50 lipofuscin granules from both strains were extracted from confocal data (Fig. 7(a)). No significant change in the emission peak or spectrum shape was found between the mouse strains. The average AF emission spectra from the confocal volume were acquired, and the emission spectrum from the *Abca4*$^{-/-}$ was elevated by a factor of ~ 3.9 relative to WT (Fig. 7(b)). The normalized spectra (Fig. 7(c)) from the confocal volume revealed that the peak emission wavelength and spectrum shape do not significantly differ between the two strains.

Electron Microscopy Images Of Rpe

Loading [MathJax]/jax/output/CommonHTML/jax.js

Electron microscopy images of RPE cell layer from WT and *Abca4*$^{-/-}$ mice are shown in Figs. 8(a) and 8(b), respectively. These axial cross-section EM images visualized all major organelles of RPE cells (melanosomes, lipofuscin, melanolipofuscin, and phagocytosed outer segments), their morphology, and population in both strains[35]. Notable differences between strains were found regarding the morphology and the density of these RPE organelles. The bottom panel of each EM image represents the mapping of the locations of each type of RPE organelles. The density (mean and SE of granules per μm^2 of imaged RPE) of lipofuscin and melanolipofuscin granules in the RPE of *Abca4*$^{-/-}$ was measured as 0.062 ± 0.011 and 0.053 ± 0.006, respectively. Conversely, a reduced density of lipofuscin (0.020 ± 0.009) and melanolipofuscin granules (0.006 ± 0.001) was measured in the WT (Figs. 8(c) and 8(d)). For calculating the area of RPE from EM images shown in 8(a) and (b), regions covering the photoreceptor outer segments were excluded. The densities of the melanosomes in the RPE of WT and *Abca4*$^{-/-}$ were found to be 0.131 ± 0.064 and 0.035 ± 0.018, respectively (Fig. 8(e)). Overall, there was a 4.7-fold increase in the number of lipofuscin/melanolipofuscin granules in *Abca4*$^{-/-}$ relative to WT, and a 3.7-fold decrease in the number of melanosomes in the *Abca4*$^{-/-}$ RPE as compared to the WT (Fig. 8(f)).

Discussion

Measurements with the dOCT system revealed variation in the directionality of scattering from the RPE and other retinal layers between *Abca4*$^{-/-}$ and WT. The melanin-free layers (ILM/NFL, ELM, and IS/OS) exhibited essentially identical directional scattering properties across the two strains. However, a striking difference was observed in the directional reflectivity of the RPE/BrM complex (Fig. 4). The RPE/BrM complex of *Abca4*$^{-/-}$ showed an increased directionality relative to the WT controls (Table 1). An increased directionality from RPE can be linked to a decreased melanin concentration in RPE cells [27]. Melanosomes are predominantly located in the apical side of the RPE cell and known as the dominant light scatters (Mie scattering) in the RPE cells. The nature of scattering (angular distribution) from melanosomes significantly depends on its shape and size (diffraction) parameter. Changes in the melanosomes, especially in the form of melanolipofuscin granules, increase their effective size parameter, causing forward scattering to become dominant from these granules[36,37]. This allows the forward propagation of the incident light with the least scattering loss in lateral directions, and results in a highly directional back-scattering from BrM[27]. Therefore, directional scattering assessment indicated that there is a relative deficit in melanosome density in the RPE cells of *Abca4*$^{-/-}$ mice relative to the WT.

In vivo SW-FAF images from *Abca4*$^{-/-}$ showed increased fluorescence intensity relative to WT, corresponding to an increased level of emission spectra (Fig. 5). Both AF images and spectral measurements confirmed that there is an increase in the accumulation of lipofuscin in the RPE cells of *Abca4*$^{-/-}$ mice. This is further validated by the qualitative and quantitative analysis of the confocal images. The *ex vivo* confocal images confirmed the excess accumulation of lipofuscin granules in the RPE of *Abca4*$^{-/-}$ (Fig. 6(b) and (d)). The peak emission wavelength measured *in vivo* (~ 590 nm for WT and ~ 645 nm for *Abca4*$^{-/-}$) was in good agreement with the *ex vivo* results (~ 635 nm). Notably, the

Loading [MathJax]/jax/output/CommonHTML/jax.js

elevation factor of the SW-FAF obtained from *Abca4*$^{-/-}$ *in vivo* (~ 3.4) is nearly the same as the elevation factor obtained from *ex vivo* spectra (~ 3.9). The comparison of the confocal images acquired with and without emission filter essentially confirmed that the non-fluorescent characteristics of the melanosomes at 488 nm excitation and identified the lipofuscin granules as the major source of FAF. There was an increase in the density of lipofuscin granules by a factor of ~ 4.2 in *Abca4*$^{-/-}$ relative to WT (Fig. 6(e) and (f)). It is noteworthy that this increase in the density of lipofuscin in *Abca4*$^{-/-}$ is correlated well with the increase in AF levels obtained from both *in vivo* and *ex vivo* spectra. The measured *in vivo* AF spectra revealed that there is a significant shift in the emission peak between WT and *Abca4*$^{-/-}$. However, no such shift was observed in the *ex vivo* spectra measured from confocal images. This relative shift observed in the *in vivo* spectra could be caused by the influence of other AF sources such as retinol or spectral filtering of the fraction of emitted light transmitted by the choroidal blood vessels, which should be further investigated.

Although confocal imaging was able to distinguish lipofuscin granules from melanosomes, it was not possible to discern a distinct population of melanolipofuscin granules in the confocal images. This might be due to the similar emission spectrum of the melanolipofuscin and lipofuscin granules. EM images, however, provided visualization of distinct melanosomes, lipofuscin, and melanolipofuscin in the RPE of both strains. Consistent with the confocal imaging, EM images confirmed the presence of excess lipofuscin and melanolipofuscin granules in the RPE of *Abca4*$^{-/-}$ relative to WT (Fig. 8(c) and 8(d)). The density of lipofuscin and melanolipofuscin (together) quantified from EM images showed that their density in *Abca4*$^{-/-}$ is approximately 4.7-fold greater than WT (Fig. 8(f)). This agrees with total number of AF granules (lipofuscin granules and melanolipofuscin) quantified (~ 4.2) from *ex vivo* confocal images. EM images also showed the reduction in the pure melanosomes in *Abca4*$^{-/-}$ by a factor of 3.7, a close to a factor of 4.7 obtained from *ex vivo* confocal images. Additionally, an increased directionality coefficient (ρ) of back-scattering between *Abca4*$^{-/-}$ and WT by a factor of 4, suggesting this coefficient is directly linked to the absolute changes in melanosome density, and thus a possible non-invasive biomarker of RPE melanin concentrations in clinical settings. The quantitative assessment of RPE melanosomes from the EM images is in good agreement with *in vivo* as well as *ex vivo* confocal results. A specific advantage of the EM images over confocal images is that they could confirm the presence of an excess amount of melanolipofuscin granules in the *Abca4*$^{-/-}$ mice. Melanolipofuscin granules are typically formed by fusing the melanosomes with lipofuscin granules under strong oxidative stress. Therefore, taking into account the fact that the melanosomes are not produced during adulthood, we hypothesize that the deficit in melanosome numbers in the *Abca4*$^{-/-}$ mice arise from the formation of melanolipofuscin from the original (and possibly damaged) melanosomes in the presence of a high density of lipofuscin granules.

Conclusion

In summary, an *in vivo* multimodal investigation based on directional scattering and fluorescence

Loading [MathJax]/jax/output/CommonHTML/jax.js

te differences between *Abca4*$^{-/-}$ mice and WT in RPE

melanosomes and lipofuscin granules. The highly directional scattering exhibited by the RPE cells of *Abca4*$^{-/-}$ mice measured with a dOCT correlated with a reduction in the RPE melanosomes. *In vivo* measured SW-FAF spectra and FAF image intensity from the same retinal region showed an increased emission from the RPE in *Abca4*$^{-/-}$ mice relative to WT. The *ex vivo* study performed on the flat-mounted RPE with confocal microscopy allowed visualization and quantification of the lipofuscin granules and melanosomes. The confocal fluorescence imaging revealed an overabundance of lipofuscin granules in the RPE cells of *Abca4*$^{-/-}$ and confirmed them as the major source of AF emission in the RPE. The *in vivo* and *ex vivo* AF emission spectra exhibited similar spectral characteristics. The degree of increase of AF emission intensity *in vivo* in *Abca4*$^{-/-}$ was in good agreement with the increased density of lipofuscins granules measured two ways *ex vivo*. Electron micrographs of the RPE cells cross-sections were used to quantify melanolipofuscin in addition to the melanosomes and lipofuscin granules. The *ex vivo* confocal microscopy and electron microscopy confirmed a reduction of the melanosomes in *Abca4*$^{-/-}$ mice predicted from decreased AF. The EM-results suggest that increased melanolipofuscin granules could be a consequence of phagocytic loss of melanosomes in *Abca4*$^{-/-}$ mice. Overall, the *in vivo* measurements correlated well with the *ex vivo* findings, highlighting the potential of such combined *in vivo* assessment using direction reflectance and SW-FAF spectra for longitudinal noninvasive monitoring of the changes in RPE melanosomes and lipofuscin granules during normal aging and the progression of outer retina disease.

Declarations

Competing interests

The author(s) declare no competing interests.

Author contributions

Design and conduct of the study (RKM, RJZ, KR, SK); data collection (RKM, KR, SK); data processing (RKM, KR, SK); manuscript preparation (RKM, RJZ); manuscript review (RKM, KR, SK, RJZ, MEB, ENP).

Acknowledgements:

Supported by NIH Grants EY02660, EY024320, EY026556, and EY012576 (NEI Core Grant), T32-EY105387, and Barr Retina Research Foundation gift to UC Davis Department of Ophthalmology.

Data availability

Images and datasets generated in this study are available from the corresponding author on reasonable request.

References

Loading [MathJax]/jax/output/CommonHTML/jax.js

1. Sparrrow, J. R., Hicks, D. & Hamel, C. P. The Retinal Pigment Epithelium in Health and Disease. *Current Molecular Medicine* **10**, 802–823, doi:http://dx.doi.org/10.2174/156652410793937813 (2010).
2. Somasundaran, S., Constable, I. J., Mellough, C. B. & Carvalho, L. S. Retinal pigment epithelium and age-related macular degeneration: A review of major disease mechanisms. *Clinical & Experimental Ophthalmology* **48**, 1043–1056, doi:https://doi.org/10.1111/ceo.13834 (2020).
3. Sparrow, J. R. & Boulton, M. RPE lipofuscin and its role in retinal pathobiology. *Experimental Eye Research* **80**, 595–606, doi:https://doi.org/10.1016/j.exer.2005.01.007 (2005).
4. Sparrow, J. R. *et al.* The bisretinoids of retinal pigment epithelium. *Progress in Retinal and Eye Research* **31**, 121–135, doi:https://doi.org/10.1016/j.preteyeres.2011.12.001 (2012).
5. Lakkaraju, A., Finnemann, S. C. & Rodriguez-Boulan, E. The lipofuscin fluorophore A2E perturbs cholesterol metabolism in retinal pigment epithelial cells. *Proceedings of the National Academy of Sciences* **104**, 11026–11031, doi:10.1073/pnas.0702504104 (2007).
6. Roberts, J. E. *et al.* The Role of A2E in Prevention or Enhancement of Light Damage in Human Retinal Pigment Epithelial Cells¶. *Photochemistry and Photobiology* **75**, 184–190, doi:https://doi.org/10.1562/0031-8655(2002)0750184TROAIP2.0.CO2 (2002).
7. Sparrow, J. R. & Duncker, T. Fundus Autofluorescence and RPE Lipofuscin in Age-Related Macular Degeneration. *Journal of Clinical Medicine* **3**, 1302–1321 (2014).
8. Delori, F. C. *et al.* In vivo measurement of lipofuscin in Stargardt's disease–Fundus flavimaculatus. *Investigative Ophthalmology & Visual Science* **36**, 2327–2331 (1995).
9. Cideciyan, A. V. *et al.* Mutations in ABCA4 result in accumulation of lipofuscin before slowing of the retinoid cycle: a reappraisal of the human disease sequence. *Human Molecular Genetics* **13**, 525–534, doi:10.1093/hmg/ddh048 (2004).
10. Lin, B. *et al.* Clinical and genetic analyses reveal novel pathogenic ABCA4 mutations in Stargardt disease families. *Scientific Reports* **6**, 35414, doi:10.1038/srep35414 (2016).
11. Lenis, T. L. *et al.* Expression of ABCA4 in the retinal pigment epithelium and its implications for Stargardt macular degeneration. *Proceedings of the National Academy of Sciences* **115**, E11120-E11127, doi:10.1073/pnas.1802519115 (2018).
12. Charbel Issa, P. *et al.* Fundus Autofluorescence in the Abca4−/− Mouse Model of Stargardt Disease—Correlation With Accumulation of A2E, Retinal Function, and Histology. *Investigative Ophthalmology & Visual Science* **54**, 5602–5612, doi:10.1167/iovs.13-11688 (2013).
13. Sparrow, J. R. *et al.* Quantitative Fundus Autofluorescence in Mice: Correlation With HPLC Quantitation of RPE Lipofuscin and Measurement of Retina Outer Nuclear Layer Thickness. *Investigative Ophthalmology & Visual Science* **54**, 2812–2820, doi:10.1167/iovs.12-11490 (2013).
14. Wang, Z., Dillon, J. & Gaillard, E. R. Antioxidant Properties of Melanin in Retinal Pigment Epithelial Cells. *Photochemistry and Photobiology* **82**, 474–479, doi:https://doi.org/10.1562/2005-10-21-RA-725 (2006).

Loading [MathJax]/jax/output/CommonHTML/jax.js

15. Sarna, T. New trends in photobiology: Properties and function of the ocular melanin — a photobiophysical view. *Journal of Photochemistry and Photobiology B: Biology* **12**, 215–258, doi:https://doi.org/10.1016/1011-1344(92)85027-R (1992).
16. Feeney-Burns, L., Burns, R. P. & Gao, C.-L. Age-related Macular Changes in Humans Over 90 Years Old. *American Journal of Ophthalmology* **109**, 265–278, doi:https://doi.org/10.1016/S0002-9394(14)74549-0 (1990).
17. Feeney, L. Lipofuscin and melanin of human retinal pigment epithelium. Fluorescence, enzyme cytochemical, and ultrastructural studies. *Investigative Ophthalmology & Visual Science* **17**, 583–600 (1978).
18. Taubitz, T., Fang, Y., Biesemeier, A., Julien-Schraermeyer, S. & Schraermeyer, U. Age, lipofuscin and melanin oxidation affect fundus near-infrared autofluorescence. *EBioMedicine* **48**, 592–604, doi:10.1016/j.ebiom.2019.09.048 (2019).
19. Bellmann, C., Rubin, G. S., Kabanarou, S. A., Bird, A. C. & Fitzke, F. W. Fundus autofluorescence imaging compared with different confocal scanning laser ophthalmoscopes. *British Journal of Ophthalmology* **87**, 1381–1386, doi:10.1136/bjo.87.11.1381 (2003).
20. Delori, F. *et al.* Quantitative Measurements of Autofluorescence with the Scanning Laser Ophthalmoscope. *Investigative Ophthalmology & Visual Science* **52**, 9379–9390, doi:10.1167/iovs.11-8319 (2011).
21. Kellner, U., Kellner, S. & Weinitz, S. Fundus autofluorescence (488 NM) and near-infrared autofluorescence (787 NM) visualize different retinal pigment epithelium alterations in patients with age-related macular degeneration. *Retina (Philadelphia, Pa.)* **30**, 6–15, doi:10.1097/iae.0b013e3181b8348b (2010).
22. Keilhauer, C. N. & Delori, F. o. C. Near-Infrared Autofluorescence Imaging of the Fundus: Visualization of Ocular Melanin. *Investigative Ophthalmology & Visual Science* **47**, 3556–3564, doi:10.1167/iovs.06-0122 (2006).
23. Wojtkowski, M. *et al.* Three-dimensional Retinal Imaging with High-Speed Ultrahigh-Resolution Optical Coherence Tomography. *Ophthalmology* **112**, 1734–1746, doi:https://doi.org/10.1016/j.ophtha.2005.05.023 (2005).
24. Adhi, M. & Duker, J. S. Optical coherence tomography – current and future applications. *Current Opinion in Ophthalmology* **24**, 213–221, doi:10.1097/ICU.0b013e32835f8bf8 (2013).
25. Lu, R.-W. *et al.* Investigation of the hyper-reflective inner/outer segment band in optical coherence tomography of living frog retina. *Journal of Biomedical Optics* **17**, 060504 (2012).
26. Huang, X.-R., Zhou, Y., Kong, W. & Knighton, R. W. Reflectance Decreases before Thickness Changes in the Retinal Nerve Fiber Layer in Glaucomatous Retinas. *Investigative Ophthalmology & Visual Science* **52**, 6737–6742, doi:10.1167/iovs.11-7665 (2011).
27. Meleppat, R. K. *et al.* Directional optical coherence tomography reveals melanin concentration-dependent scattering properties of retinal pigment epithelium. *Journal of Biomedical Optics* **24**,

Loading [MathJax]/jax/output/CommonHTML/jax.js

28. Song, G. *et al.* Multimodal Coherent Imaging of Retinal Biomarkers of Alzheimer's Disease in a Mouse Model. *Scientific Reports* **10**, 7912, doi:10.1038/s41598-020-64827-2 (2020).
29. Chen, H. *et al.* Quantitative analysis of retinal layers' optical intensities on 3D optical coherence tomography for central retinal artery occlusion. *Scientific Reports* **5**, 9269, doi:10.1038/srep09269 (2015).
30. Thevenaz, P., Ruttimann, U. E. & Unser, M. A pyramid approach to subpixel registration based on intensity. *IEEE Transactions on Image Processing* **7**, 27–41, doi:10.1109/83.650848 (1998).
31. Zhang, P. *et al.* In vivo wide-field multispectral scanning laser ophthalmoscopy–optical coherence tomography mouse retinal imager: longitudinal imaging of ganglion cells, microglia, and Müller glia, and mapping of the mouse retinal and choroidal vasculature. *Journal of Biomedical Optics* **20**, 126005 (2015).
32. Meleppat, R. K. *et al.* In Situ Morphologic and Spectral Characterization of Retinal Pigment Epithelium Organelles in Mice Using Multicolor Confocal Fluorescence Imaging. *Investigative Ophthalmology & Visual Science* **61**, 1–1, doi:10.1167/iovs.61.13.1 (2020).
33. Ding, J. D., Salinas, R. Y. & Arshavsky, V. Y. Discs of mammalian rod photoreceptors form through the membrane evagination mechanism. *The Journal of cell biology* **211**, 495–502, doi:10.1083/jcb.201508093 (2015).
34. Sezgin, M. & Sankur, B. Survey over image thresholding techniques and quantitative performance evaluation. *Journal of Electronic Imaging* **13** (2004).
35. Conley, S. M. *et al.* Increased cone sensitivity to ABCA4 deficiency provides insight into macular vision loss in Stargardt's dystrophy. *Biochimica et Biophysica Acta (BBA) - Molecular Basis of Disease* **1822**, 1169–1179, doi:https://doi.org/10.1016/j.bbadis.2011.10.007 (2012).
36. Song, W., Zhang, L., Ness, S. & Yi, J. Wavelength-dependent optical properties of melanosomes in retinal pigmented epithelium and their changes with melanin bleaching: a numerical study. *Biomed. Opt. Express* **8**, 3966–3980, doi:10.1364/BOE.8.003966 (2017).
37. Bhandari, A., Hamre, B., Frette, Ø., Stamnes, K. & Stamnes, J. J. Modeling optical properties of human skin using Mie theory for particles with different size distributions and refractive indices. *Opt. Express* **19**, 14549–14567, doi:10.1364/OE.19.014549 (2011).

Figures

Loading [MathJax]/jax/output/CommonHTML/jax.js

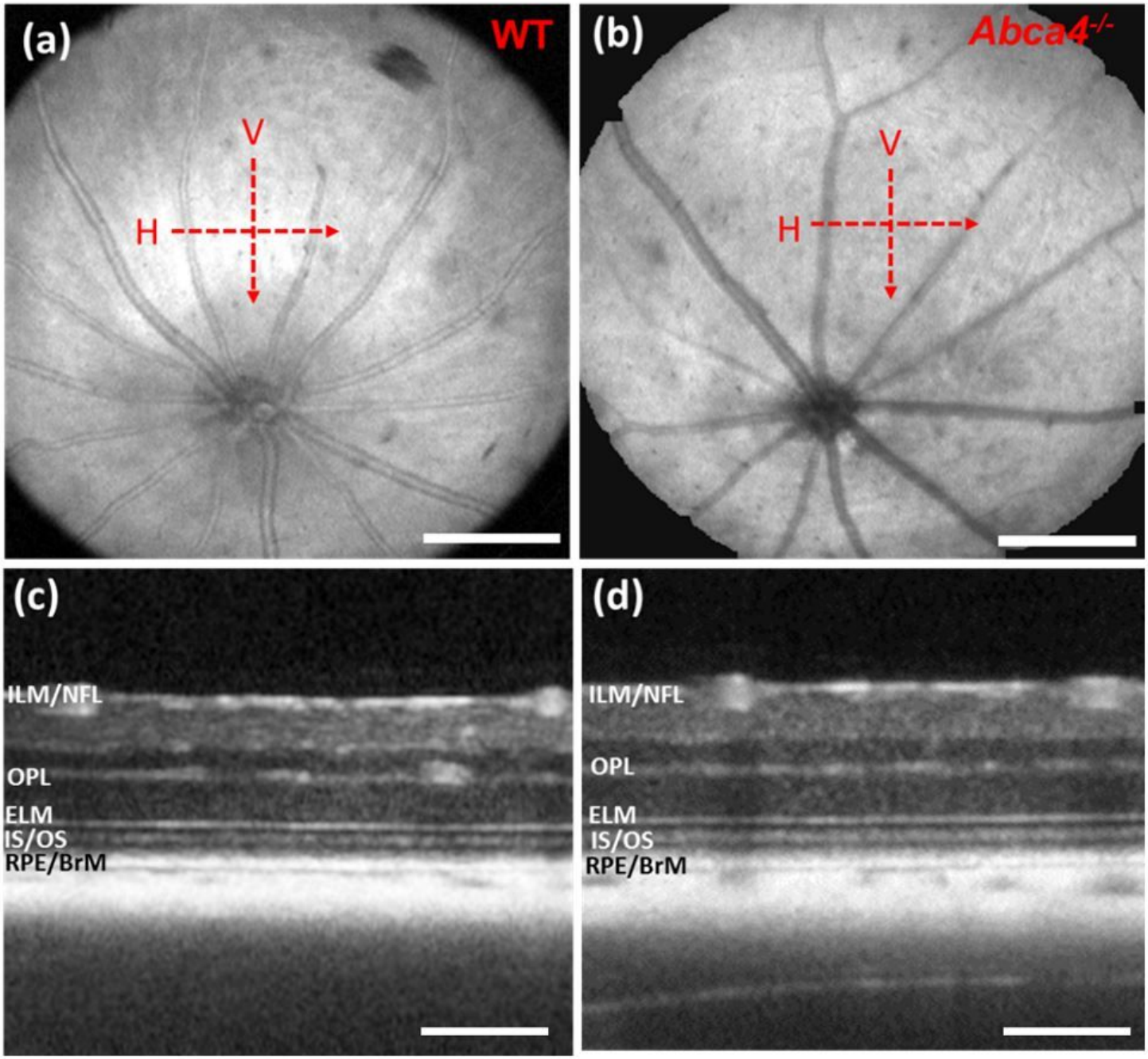

Figure 1

Representative enface OCT fundus and B-scan images. (a) Enface fundus image of a WT mouse. (b) Enface fundus image of an Abca4-/- mouse. Red dashed arrows show the location and direction of OCT scanning in horizontal (H) and vertical (V) directions. (c) Averaged B-scan acquired (zero-degree incident angle) from WT mouse along H direction. (d) Averaged B-scan acquired (zero-degree incident angle) from an Abca4-/- mouse along H direction shown. Scale bar (a) and (b): 400 μm; Scale bar (c) and (d): 200 μm.

Loading [MathJax]/jax/output/CommonHTML/jax.js

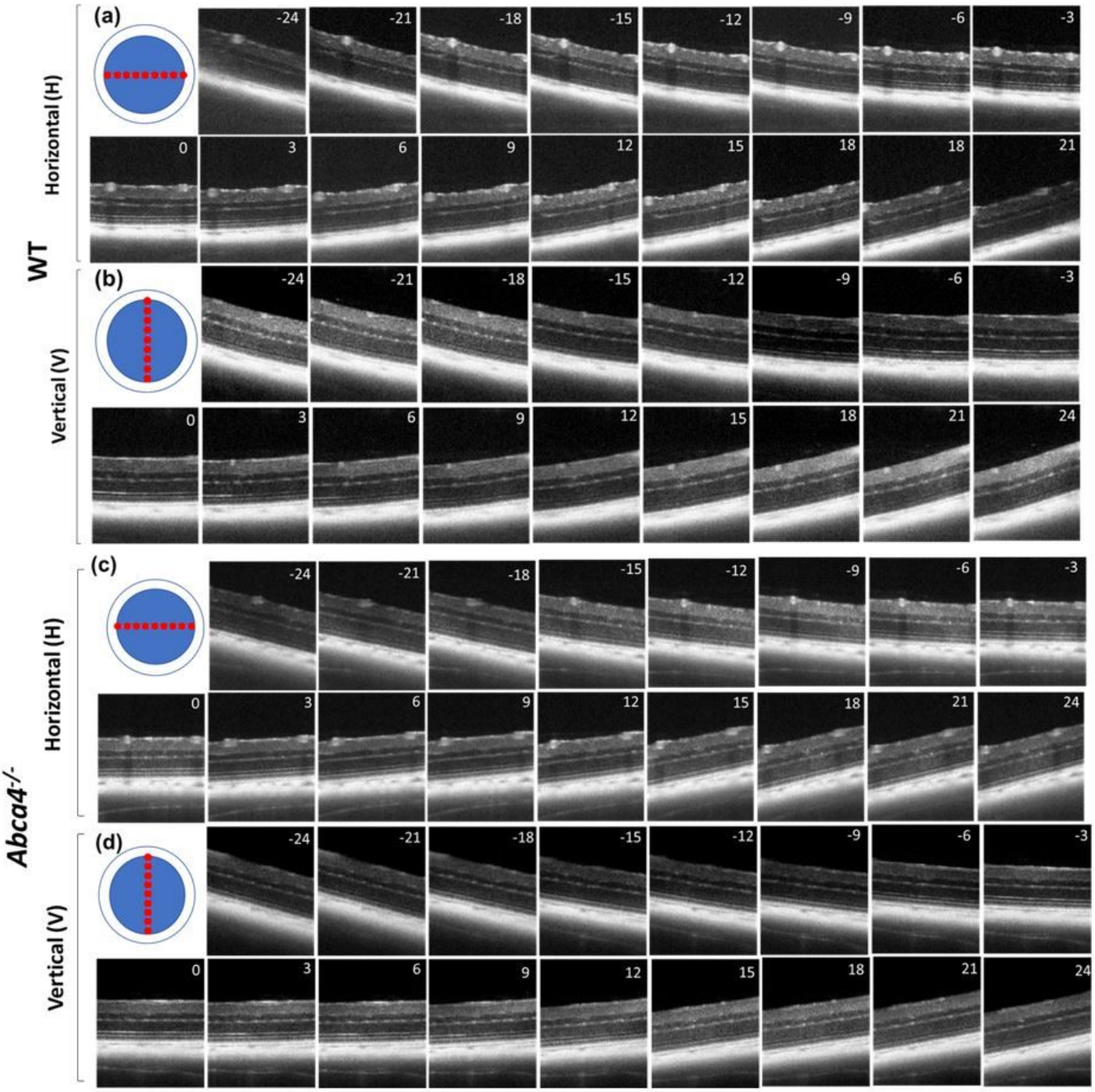

Figure 2

Averaged directional OCT B-scans (log scale) acquired from a WT and Abca4-/- mouse. (a) B-scans from WT mouse corresponding to 17 beam entry positions along H direction. (b) B-scans from WT mouse corresponding to 17 beam entry positions along V direction. (c) B-scans from Abca4-/- mouse corresponding to 17 beam entry positions along H direction. (d) B-scans from Abca4-/- mouse corresponding to 17 beam entry positions along V direction. The number provided in each B-scan represents the incidence angle of retinal illumination.

Loading [MathJax]/jax/output/CommonHTML/jax.js

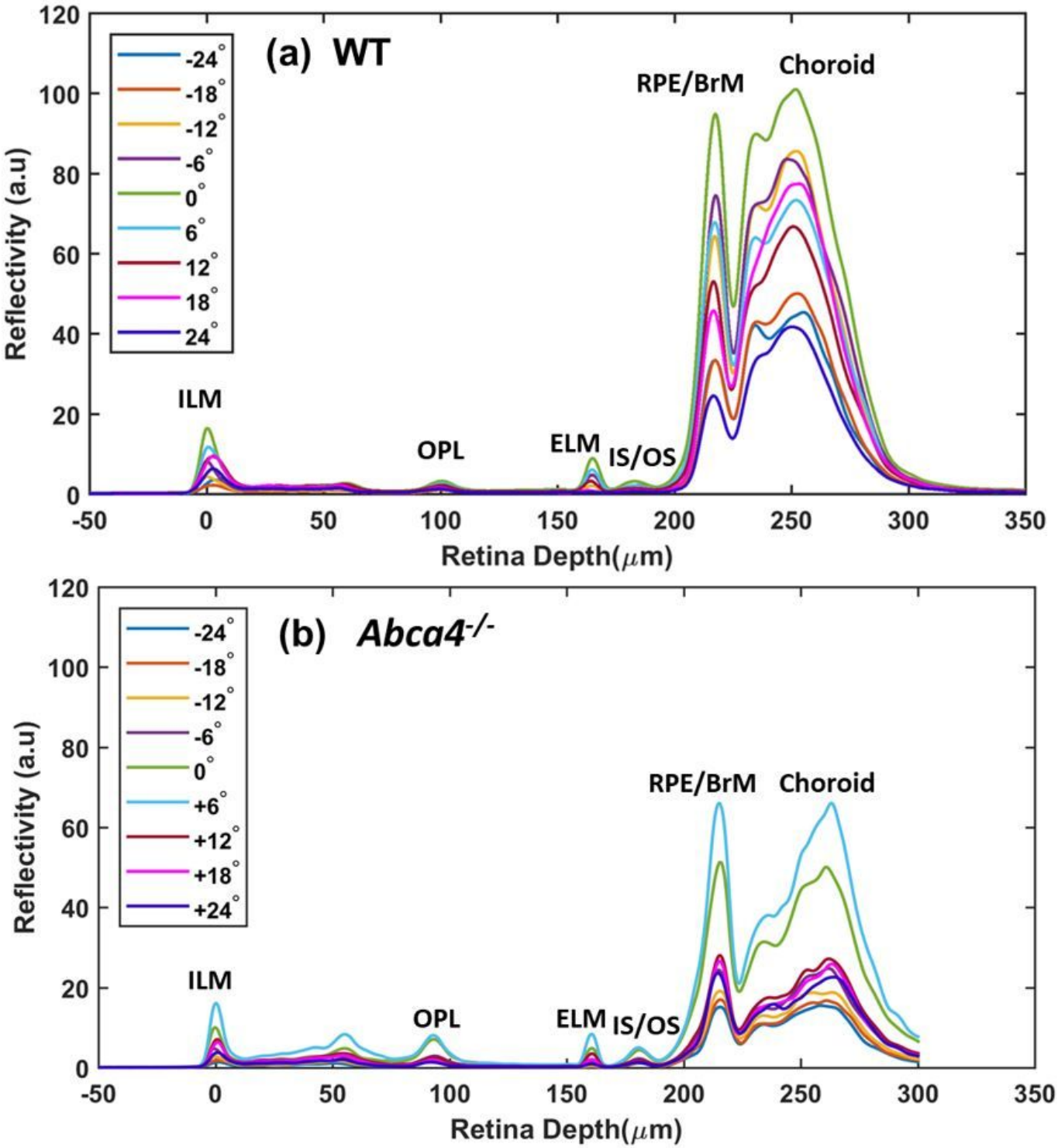

Figure 3

Representative average A-scans (linear scale) obtained for different angles of incidence from WT and Abca4-/- mice. (a) Average A-scans obtained along the H direction from a WT mouse. (b) Average A-scans obtained along H direction from an Abca4-/- mouse.

Loading [MathJax]/jax/output/CommonHTML/jax.js

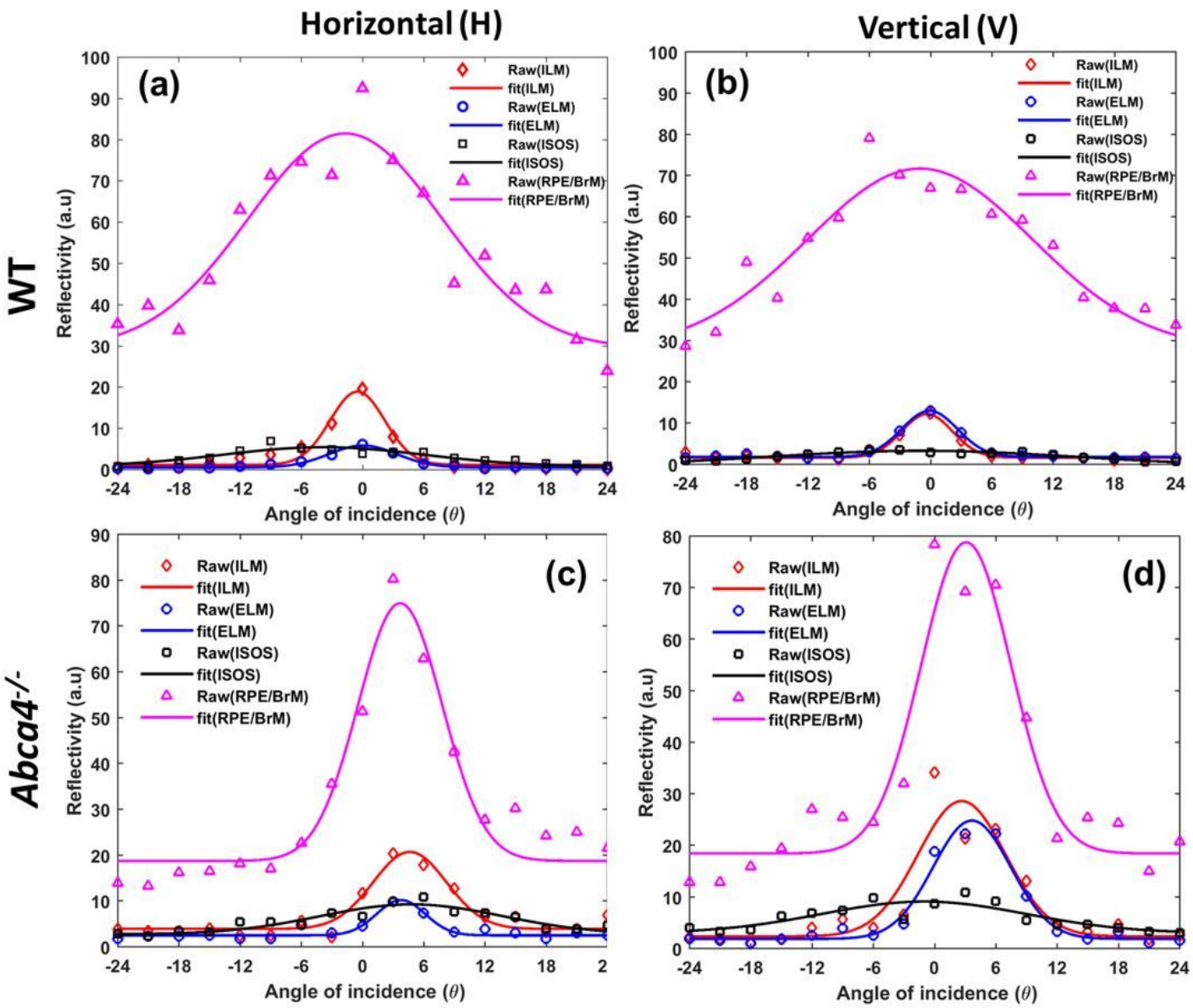

Figure 4

Gaussian fits to the dOCT based layer-specific and incident angle-dependent reflectivity profiles for WT (a & b) and Abca4-/- mice (c & d). (a) and (c) reflectance of different retina layers as a function of angle of incidence measured along H. (b) and (d) reflectance of different retina layers as a function of angle of incidence measured along V direction.

Loading [MathJax]/jax/output/CommonHTML/jax.js

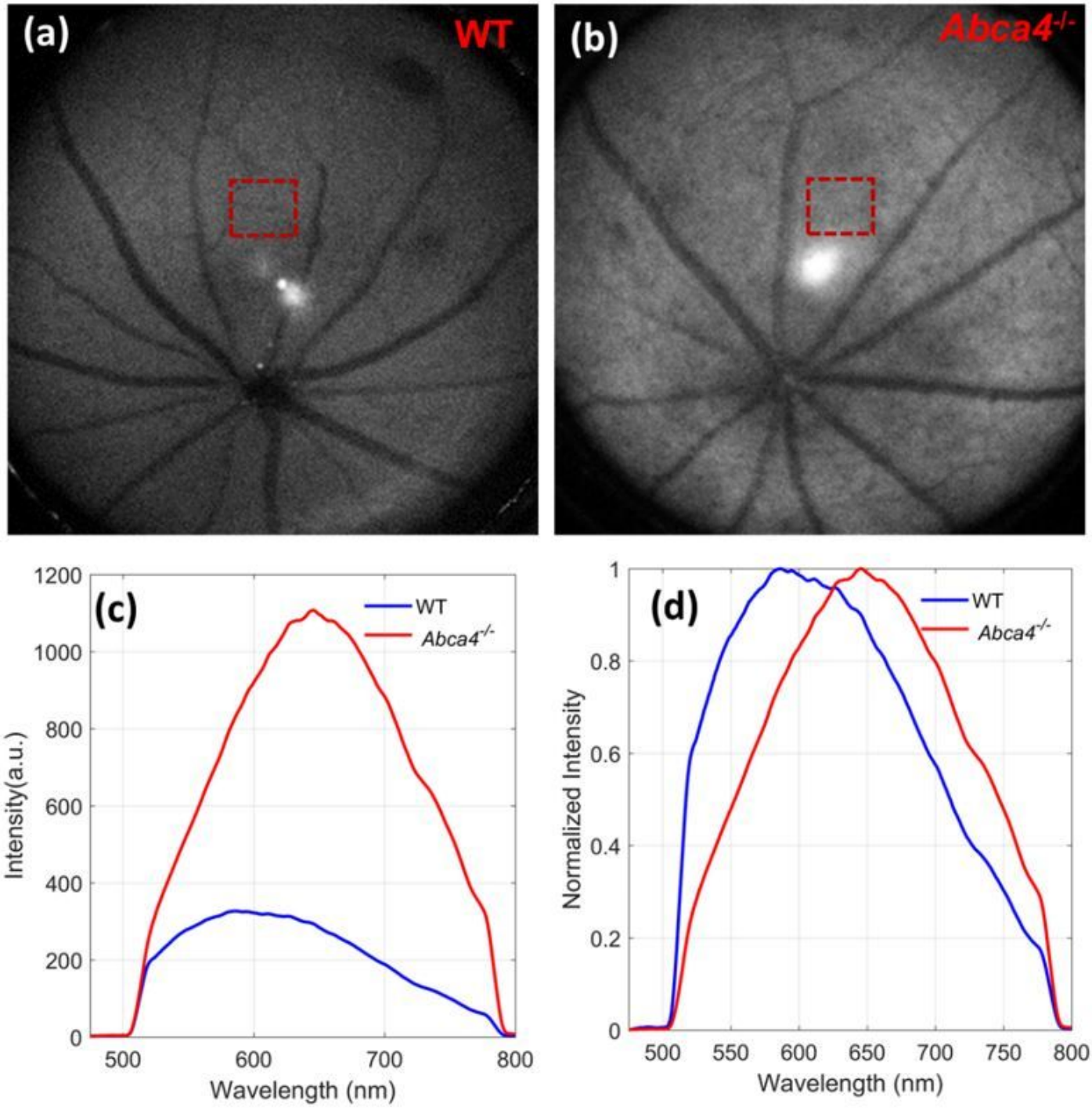

Figure 5

In vivo FAF images and emission spectra acquired with 488 nm excitation. FAF image of (a) WT and (b) Abca4-/- mice. (c) Absolute emission spectra measured from WT control and Abca4-/- mice. (d) Normalized emission spectra from (c). Dashed red rectangles in (a) and (b) show the locations where AF spectra were measured. (The sharp decline in fluorescence in (c) and (d) at about 510 nm is due to the dichroic cut-off filter).

Loading [MathJax]/jax/output/CommonHTML/jax.js

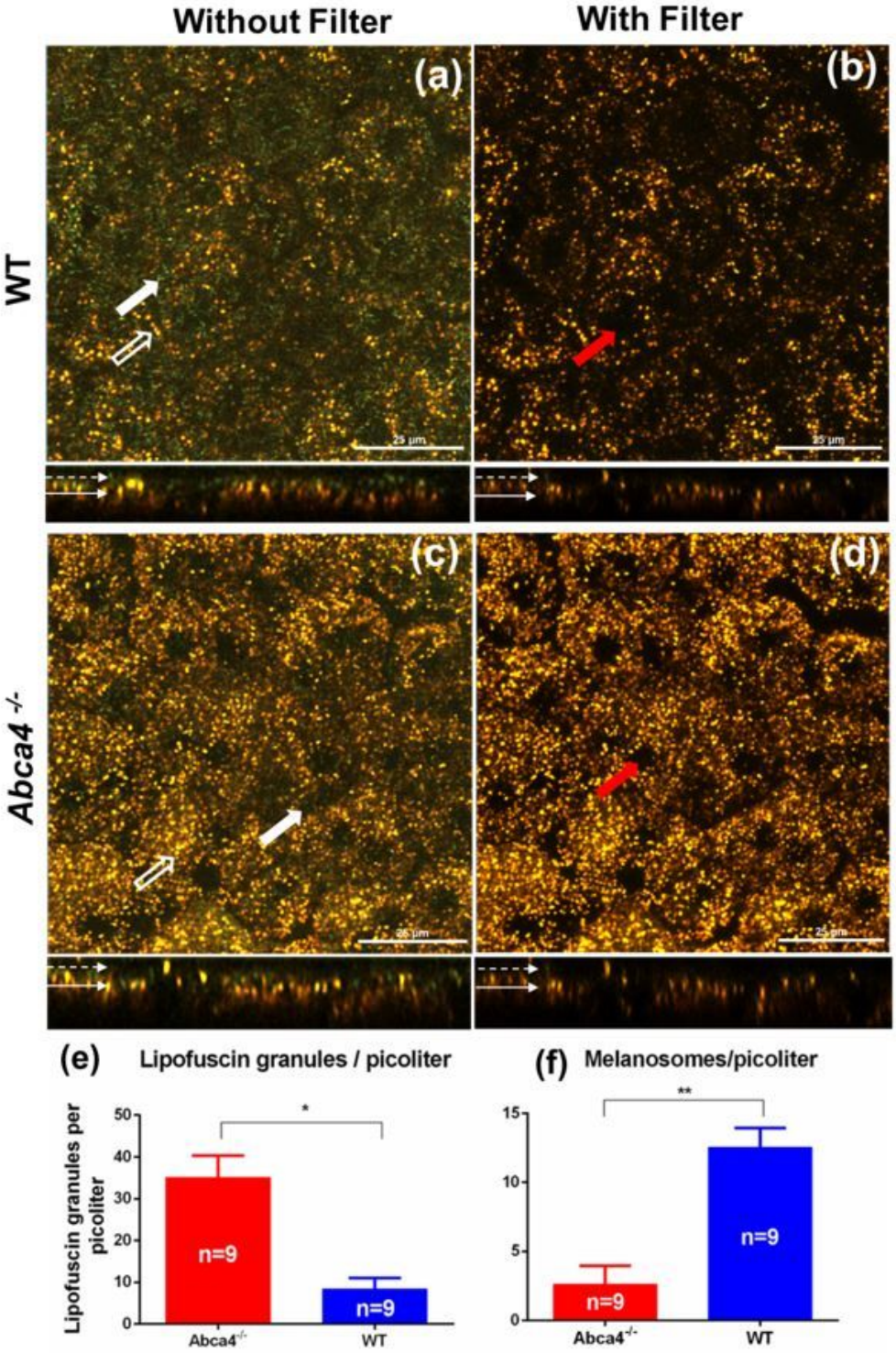

Figure 6

Representative confocal images of flat-mounted RPE from WT and Abca4-/-mice. (a),(c) Confocal images of RPE cell mosaic acquired without emission filter. (b),(d) Confocal images of RPE cell mosaic acquired with emission filter. (e) and (f) bar graph showing the density (number of granular per picoliter) of lipofuscin and melanosomes measured from the confocal volumes. The average number of lipofuscin

Loading [MathJax]/jax/output/CommonHTML/jax.js

from 9 confocal volumes per strain (three confocal volumes

from one eye of three mice from each strain). White solid arrows show the melanosomes. The hollow arrow shows lipofuscin granules. The red arrow shows the nuclei in the RPE cells. The bottom panels show the side views of the RPE volume acquired. The dotted arrow in the bottom panel shows the apical side of the RPE cells, whereas the solid arrow indicates the basal side of the RPE. (*p<0.001,**p < 0.001). Scale bar: 25 μm.

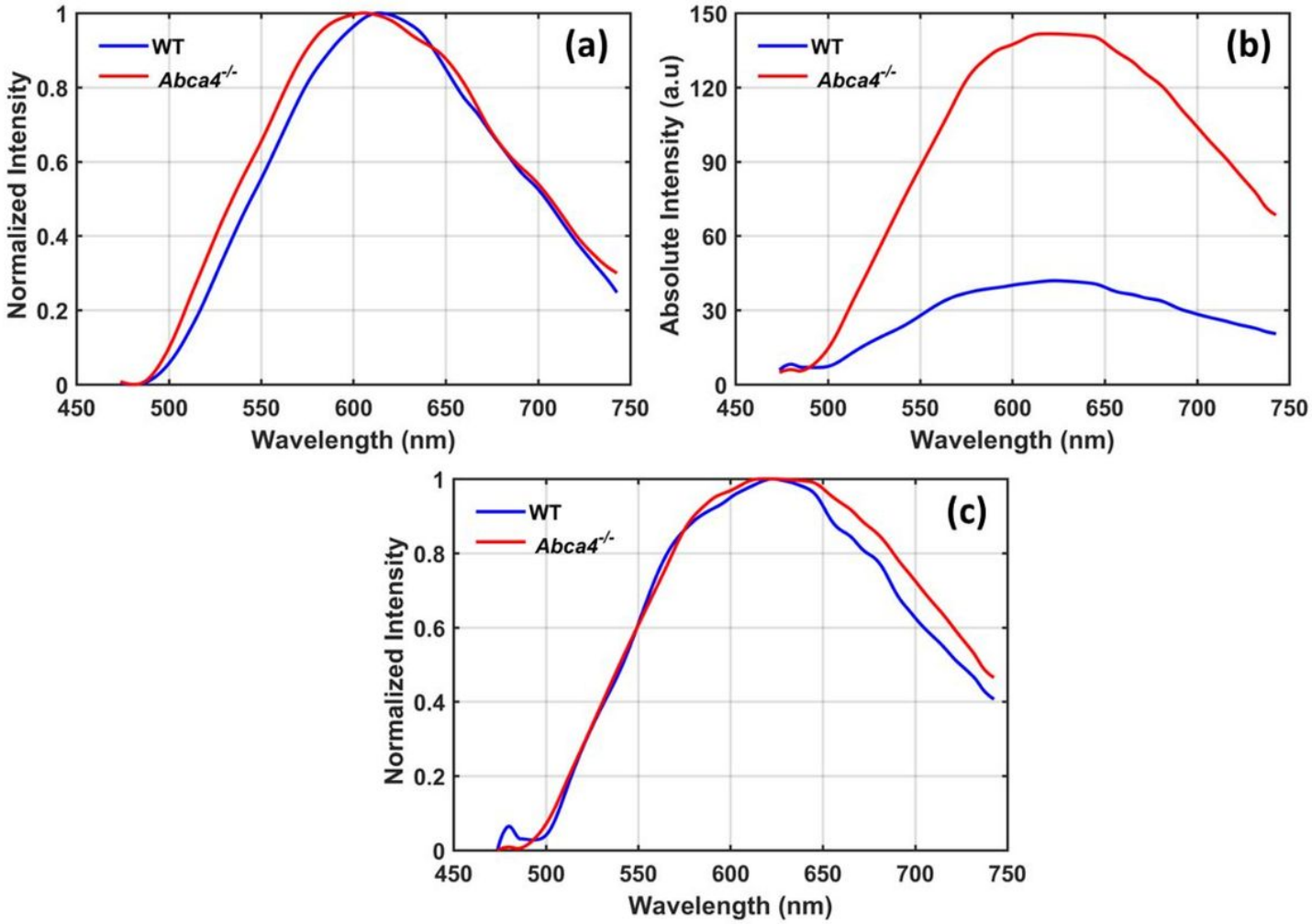

Figure 7

AF emission spectra obtained with ex vivo confocal imaging for an excitation wavelength of 488 nm. (a) Average emission spectra acquired from 50 lipofuscin granules (Spectra were and normalized to the emission peak). (b) Average emission spectra measured from the whole confocal volume with identical excitation power. (c) Normalized spectra from (b)

Loading [MathJax]/jax/output/CommonHTML/jax.js

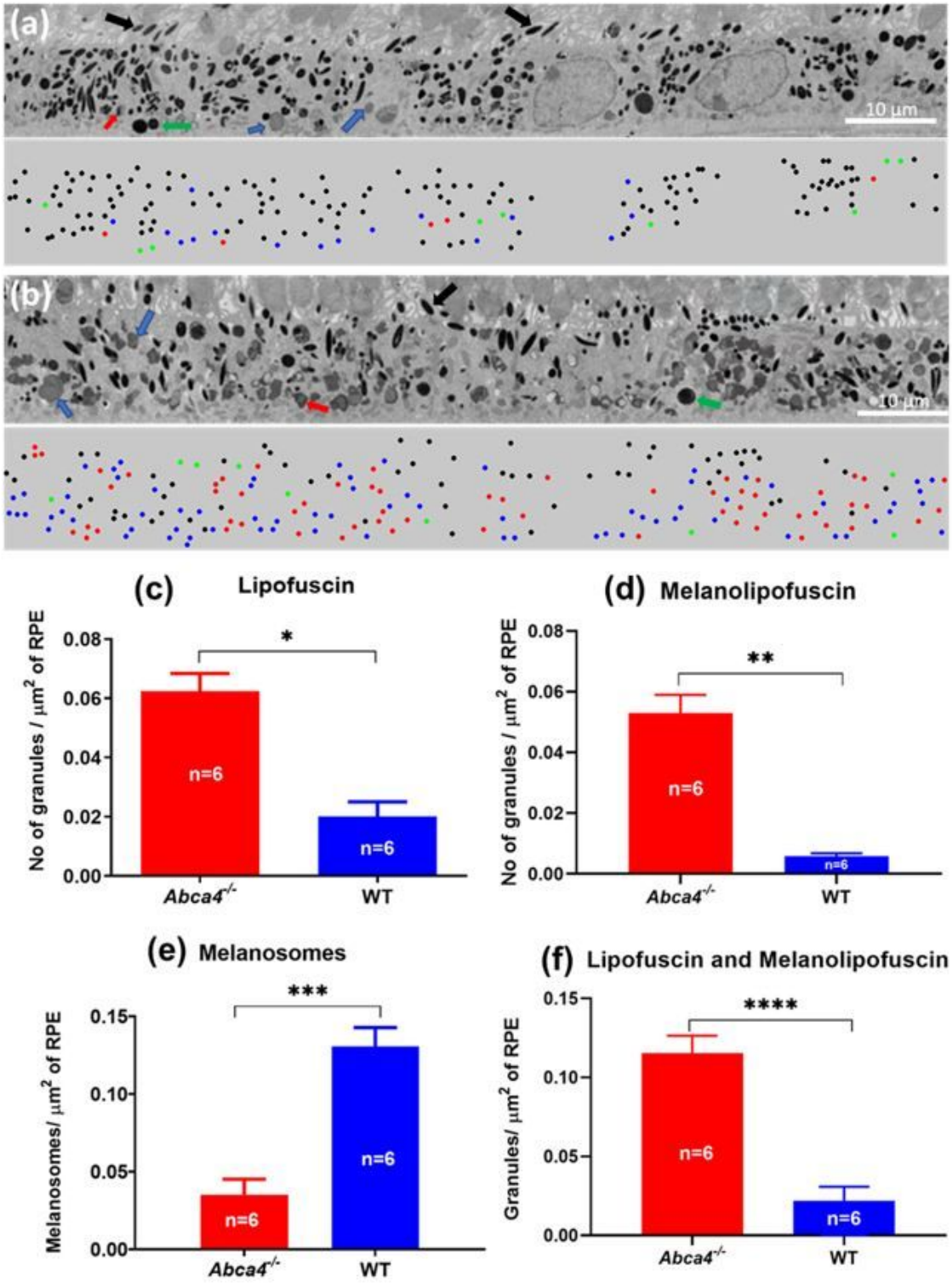

Figure 8

Representative EM images showing RPE cell layer and RPE organelles. (a) RPE cell layer of WT mouse. (b) RPE cell layer Abca4-/ mouse. The bottom panel of (a) and (b) are the color-coded classified organelles showing their location and count. Number of granues per µm2 calculated for (c) lipofuscin, (d) melanolipofuscin, (e) melnaosomes, and (f) lipofuscin and melanolipofuscin. The values shown are

Loading [MathJax]/jax/output/CommonHTML/jax.js

ere quantified per strain (one eye each from 2 animals per

group were analyzed and 3 images per eye were counted). Black arrows and dots: Melanosomes; Blue arrows and dots: lipofuscin; Green arrows and dots: phagocytosed outer segments; red arrows and dots: melanolipofuscin (*$p<0.001$, **$p<0.01$, ***$p<0.001$, ***$p<0.001$)

Loading [MathJax]/jax/output/CommonHTML/jax.js